Observation of ion scale fluctuations in the pedestal region during the edge-localized-mode cycle on the National Spherical Torus Experiment[a]

A. Diallo,[1,b] G. J. Kramer,[1] D. R. Smith,[2] R. Maingi,[3] R. E. Bell,[1] W. Guttenfelder,[1] B. P. LeBlanc,[1] M. Podestà,[1] G. J. McKee,[2] and R. Fonck[1,2]

[1]Princeton Plasma Physics Laboratory, Princeton, New Jersey 08540, USA
[2]Departments of Engineering Physics and Physics, University of Wisconsin, Madison, Wisconsin, USA
[3]Oak Ridge National Laboratory, Oak Ridge, Tennessee, 37831 USA

Characterization of the spatial structure of turbulence fluctuations during the edge localized mode cycle in the pedestal region is reported. Using the beam emission spectroscopy and the correlation reflectometry systems, measurements show spatial structure—$k_\perp \rho_i^{\text{ped}}$—ranging from 0.2 to 0.7 propagating in the ion diamagnetic drift direction at the pedestal top. These propagating spatial scales are found to be anisotropic and consistent with ion-scale microturbulence of the type ion temperature gradient and/or kinetic ballooning modes. © 2013 American Institute of Physics. [http://dx.doi.org/10.1063/1.4773402]

I. INTRODUCTION

Performance projections for the International Thermonuclear Experimental Reactor (ITER)[1] have emphasized the relation between fusion gain of the burning plasma core and the edge plasma parameters in the high confinement (H-mode) regime. This regime arises from the formation of an edge transport barrier and the generation of a "near-step" in the edge plasma profile, commonly referred to as the "pedestal." Using multiple transport models, the fusion performance for ITER has been predicted to be proportional to the pedestal temperature height squared at fixed density (effectively proportional to the pressure pedestal height).[2] Due to this strong dependence, the pedestal height emerges as a control knob for fusion performance. However, increasing the pedestal height is limited by a class of instabilities known as edge localized modes (ELM).[3] The peeling ballooning theory[3–5] is the leading candidate in explaining the process that limits the increase of the pedestal height. This theory constitutes the backbone of the recently developed predictive model recently developed predictive model (EPED).[6,7] which is based on the hypothesis that the pedestal pressure height is limited by the peeling ballooning instability, and the pressure gradient is limited by kinetic ballooning modes (KBMs). This model has successfully predicted the pedestal height and width in several standard aspect ratio ($R/a \sim 3$) tokamak experiments.[7] In low aspect ratio tokamaks such as National Spherical Torus Experiment (NSTX), however, the applicability of the EPED model is not yet established. Analysis pertaining to the various elements of the EPED hypothesis are conducted separately.

A wide range of ELM (type I, type II, type III, and grassy type V) have been observed[9] in NSTX, creating a natural testbed for evaluation of peeling-ballooning stability limits. Moreover, the use of lithium wall coatings to gradually suppress ELM[10,11] has provided experimental examples of improving edge stability with increasing lithium deposition.[12] Detailed edge stability analysis showed[13,14] that type I ELMy discharges were near the kink/peeling stability boundary, while ELM-free discharges were farther from that boundary. The key to improving the edge stability was a resilient temperature gradient in the edge, coupled with reduced density gradient from lithium pumping and a reduction of edge particle and energy transport.[15]

Furthermore, the pedestal structure (e.g., height, width, and gradient) dynamics during the inter-ELM phase have been characterized in NSTX.[16] Summarized in Ref. 16 is the pedestal structure evolution during a type I ELM cycle. More specifically, the pedestal height was found to build up, and in some cases, saturate during the last 40% of the cycle. Similarly, the pedestal width increased concomitant with the pedestal height, with the pressure gradient clamped early in the ELM cycle. The saturation of the pedestal height, late in the ELM cycle, is in contrast with some of the DIII-D observations where this saturation occurred in the first 20% of the ELM cycle.[17] In MAST—Mega Ampere Spherical Tokamak (with a similar aspect ratio to NSTX), however, no saturation of the pedestal height was observed.[18] In NSTX, both trends are observed at different I_p. More specifically, at high plasma current ($I_p \sim 1.2$ MA), we observed a continuous rise of the pedestal height until the onset of ELM, similar to the pedestal height dynamics in the MAST device. These characteristics of the NSTX pedestal height dynamics are also consistent with the peeling ballooning theory description of the ELM cycle.

In addition to experimentally characterizing the pedestal dynamics during the ELM cycle, the pedestal width scaling[16] with $(\beta_{\text{pol}}^{\text{ped}})^{1/2}$ ($\beta_{\text{pol}}^{\text{ped}} = 2\mu_0 P_{\text{ped}}/B_\theta^2$; P_{ped} is the pedestal height, B_θ represents the poloidal field) showed similar scaling with $(\beta_{\text{pol}}^{\text{ped}})^{1/2}$ as reported in other tokamaks. This scaling is expected if the pressure gradient is limited by the KBM.[6] While this scaling is a good description of width scaling observed in systematic parameter scans over multiple tokamaks, the observed width in NSTX is 2.4 and 1.7 times wider than DIII-D and C-Mod, and MAST, respectively.

KBMs are electromagnetic instabilities driven by strong pressure gradients associated with H-mode pedestals. KBMs are long wavelength modes similar in spatial scale to ion temperature gradient (ITG) modes.[19] Recently in the DIII-D tokamak, fluctuation measurements using the beam emission spectroscopy (BES) system have shown that high frequency coherent modes exist in high pedestal pressure quiescent H-mode[20] conditions and that these modes exhibit characteristics expected for KBMs in the linear regime.[21] These characteristics include propagation in the ion diamagnetic drift direction and spatial scales of a few centimeters in the pedestal region. While an experimental identification of the KBM instabilities is challenging, as it requires high spatial and temporal resolution of the local turbulence in the pedestal, there is growing evidence of the existence of KBM and microtearing modes in the pedestal region using gyrokinetic simulations,[22,23] as well as experimental observations not inconsistent with KBM.[24]

In MAST, detailed gyrokinetic calculations have indicated the coexistence of both KBMs[22] and microtearing modes during the pedestal evolution near the pedestal top ($\psi_n \sim 0.96$).[22] In NSTX, nonlinear simulations using GYRO[25] clearly show the existence of KBMs near the pedestal top ($r/a \sim 0.8$) in high collisionality discharges.[26] Thus, KBMs and microturbulence in general are clearly predicted to exist near or at the pedestal top. The question, however, remains: Do microinstabilities physically play a role in the inter-ELM pedestal evolution? To address this question, it is crucial to gain some insight into the fluctuation characterization in the pedestal region during the inter-ELM phase.

This paper focuses on the turbulence characterization during the inter-ELM phase in the pedestal region and is divided into three sections. Section II describes the experimental conditions during the ELMy discharges. Section III discusses the fluctuation characterizations in the pedestal region during the inter-ELM phase. Finally, in section IV, a summary and discussion are given on the theoretical implications of the microturbulence in the pedestal region and possible links with the pedestal structure evolution.

II. EXPERIMENTAL CHARACTERIZATION

Experiments were performed on NSTX to characterize the inter-ELM evolution of the pedestal structure. NSTX[8] is a medium-sized low aspect-ratio spherical torus (ST) of major radius $R \sim 0.85$ m, minor radius $a \leq 0.67$ m, and $B_\varphi \leq 0.55$ T. H-mode discharges are typically obtained using neutral beam injection (NBI) heating with powers up to 6 MW. The discharges studied used a marginally double-null divertor configuration, with the plasma slightly biased down ($\delta_r^{sep} \sim -5$ mm, where δ_r^{sep} represents the radial distance between the upper and the lower X-points mapped to the outer midplane), and a bottom triangularity $\delta_{bot} \sim 0.6$. The upper triangularity was typically kept at 0.4 while the elongation κ varied between 2.3 and 2.4.

Figure 1 shows a discharge example at constant NBI power, the total stored energy (W_{mhd}), and divertor light emission signals. Amounts of lithium evaporated less than 50 mg between discharges are typically deposited on the
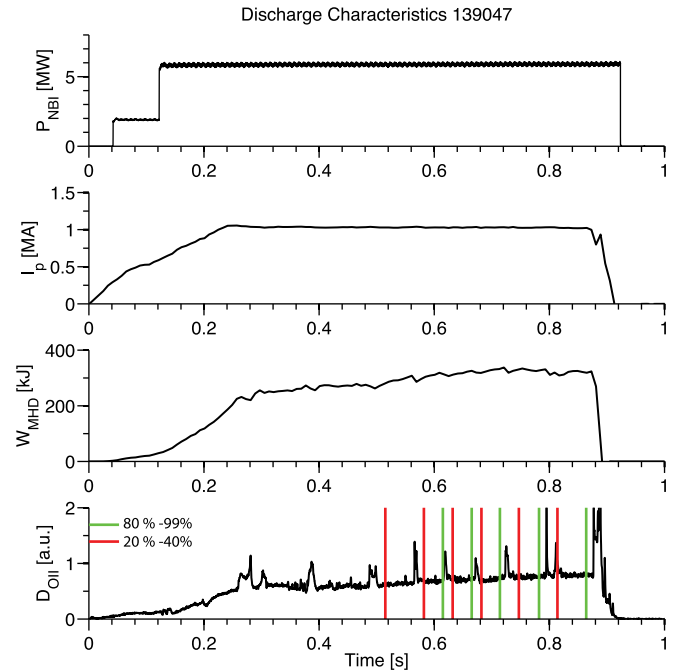

FIG. 1. Discharge characteristics. From top to bottom are the evolution of injected power, plasma current, total stored energy, and D-OII trace (indicating the ELMs). On the bottom plot are shown the two time slices representing the early and late phases of ELM cycle.

plasma facing component to ensure reproducible ELM, while thick coating of lithium (>200 mg) enables access to ELM-free regimes.[10–13]

The main diagnostics utilized to characterize the pedestal parameters were the mid-plane Thomson scattering system (multi-point Thomson scattering—MPTS) for electron density (n_e) and electron temperature (T_e) sampled at 60 Hz,[27] the C^{6+} charge-exchange recombination spectroscopy[28] for providing the carbon density and ion temperature T_i with a 10 ms time resolution, and the divertor light emissions for identifying ELM.

Using multiple fractional time windows of ELM cycles, the kinetic profiles (MPTS and CHERS) are reduced by generating composite quasi-equilibrium edge plasma profiles.[29] The composite edge profile of the electron density during the early phase of an ELM cycle is shown in Figure 2. Here and in the remainder of the text, the "top" of the pedestal is located at half the pedestal width (toward the magnetic axis) from the symmetry point or peak gradient. This definition is determined from the tangent hyperbolic (tanh) fit of the electron density and temperature edge profiles. The pedestal height is generally determined at the pedestal top. The ion temperature profiles do not show a pedestal and therefore are simply "spline-fitted." In addition, throughout the analysis reported below, a tanh-fit for the electron density profile is assumed.

III. EDGE FLUCTUATION SPATIAL CHARACTERIZATIONS IN THE PEDESTAL REGION DURING THE INTER-ELM PHASE

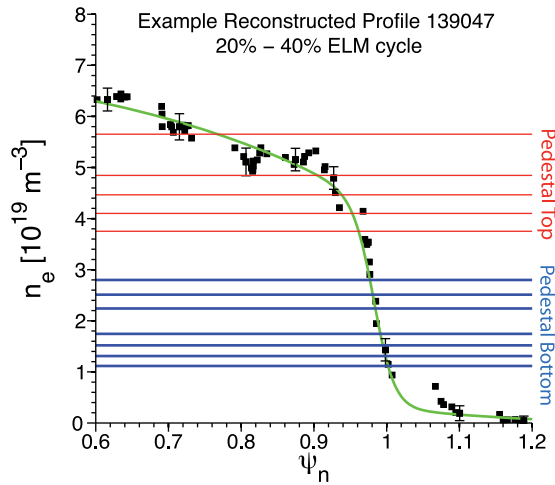Inter-ELM edge fluctuations in the pedestal region are characterized using the correlation reflectometry[30] and the

FIG. 2. Example of a composite profile, in normalized flux ψ_n, of the electron density during the early phase of the type I ELM normalized poloidal flux. Squares represent the data points and the line represents the best fit using a modified hyperbolic tangent. The horizontal lines display the cutoff densities of the reflectometer in the pedestal region.

BES diagnostic systems.[31] These two diagnostics enable the determination of the radial and poloidal spatial structure of fluctuations in the pedestal region, in addition to their propagation in the poloidal direction.

A. Characterization of the radial spatial structure

Characterization of the edge density fluctuations in the radial direction during the inter-ELM phase is performed using the fixed-frequency reflectometer system. The 16 channel array operates over a frequency range from 30 to 75 GHz, with equivalent O-mode cutoff densities ranging from 1.1×10^{19} to 6.9×10^{19} m^{-3}, allowing excellent coverage of the pedestal region of high performance plasmas in NSTX.[30] The unique capability of this array has been exploited to characterize the spatial scales of the density fluctuations in the pedestal region during the inter-ELM phase.

Measurements of the inter-ELM density fluctuations are performed using correlation reflectometry.[32] The coherency,[33] γ, between two signals S_1 and S_2 probing radially disjoint locations of the density profile, was calculated in the frequency domain using a Fourier method. we show in the appendix that coherency is equivalent to correlation estimates in time domain. Throughout this section, the reflectometer quadrature signal (real and imaginary components) is used to compute γ (see Ref. 34 for a review on the use of quadrature signals in correlation reflectometry). Examples of the quadrature power spectra emphasizing broadband fluctuations are displayed in Figure 3(a) and comparison with BES typical power spectra is shown in Figure 3(b). These broadband fluctuations contrast with phase fluctuation spectra shown in Fig. 8 of Ref. 16, which displays coherent features in the phase fluctuations during the inter-ELM phase. From the multiple pairwise cross-correlation, a radial correlation length λ^r_{obs} in the radial direction is determined. Note that λ^r_{obs} is a convolution of the instrument function and the density fluctuation levels ($\delta n/n$) and turbulence radial correlation length (λ^r_{turb}). Hence, λ^r_{obs} is in general not equal to λ^r_{turb}. Since our goal is to determine λ^r_{turb} for comparison with other

diagnostics, a full wave model is required to unfold the instrument function.

The accurate determination of the correlation lengths depends on good density profile reconstruction, especially when the pedestal region is undersampled. To obtain meaningful correlation length measurements using the correlation reflectometry system, it is important to have an accurate knowledge of the relative distance between reflection points. While the Thomson scattering system on NSTX gives measurements of the density profiles across the plasma, the pedestal region is sometimes undersampled depending on the outer gap set by the plasma control system. The optimal pedestal spatial resolution is generally obtained for an outer-gap of 10 cm on NSTX. To minimize the lack of spatial resolution in the pedestal, we use composite density profiles between ELM cycles and fit them with the functional form tanh (see Fig. 2). This approximation has been tested against single time-slice profiles and showed accuracy better than 10% in the gradient region, and 20% at the pedestal top. These errors are propagated in our estimates of the measured correlation lengths in the pedestal region, and contribute to the overall errors in the observed correlation lengths. The other source of errors is statistical errors originating from the use of multiple time slices for each ELM cycle, which yield in correlation lengths uncertainties ranging between 2 and 4 mm.

Figure 4 displays the correlation functions early during the ELM cycle and just prior to the ELM onset for the pedestal top and steep gradient region. Correlation lengths are determined from the e-folding lengths of the Gaussian or exponential fits to the measured correlation functions. We find that best fits for the data are obtained using Gaussian functions at pedestal bottom. On the other hand, at the pedestal top, an exponential fit is more adequate than a Gaussian fit. This change in the functional form is not understood and could hide or reflect changes in the turbulence characteristics between the two regions (top and bottom of the pedestal).

For the quantitative interpretation of the fluctuation magnitude and radial correlation length, the 2D full wave simulation using FWR2D[35] has been performed. This code has been validated through detailed benchmarking to Langmuir probe measurements in laboratory.[35–37] The full wave simulation using FWR2D is utilized with realistic antenna geometry and with experimental density profiles and reconstructed equilibria for the plasma shape. In addition, the full wave analysis covered most of the plasma, and density fluctuations are assumed constant across the plasma profiles. This assumption is considered reasonable since the analysis targeted the pedestal region. The code uses a Gaussian antenna radiation pattern, and the density fluctuation is simulated by a 2D density distribution (radial and poloidal). Given a choice of $\delta n/n$, $\langle k_\perp \rangle$, and spread, thousands of runs are performed to form a statistical ensemble of randomly varying quadrature signals, which are then used for computing the correlation function for comparison with experimental data.

Figure 5 displays a map of the turbulence parameters ($\delta n/n$, $\langle k^r_{turb} \rangle = 2/\lambda^r_{turb}$). The horizontal axis represents λ^r_{obs} and the vertical axis indicates the associated coherency. This map provides the corresponding $\delta n/n$ and average eddy size
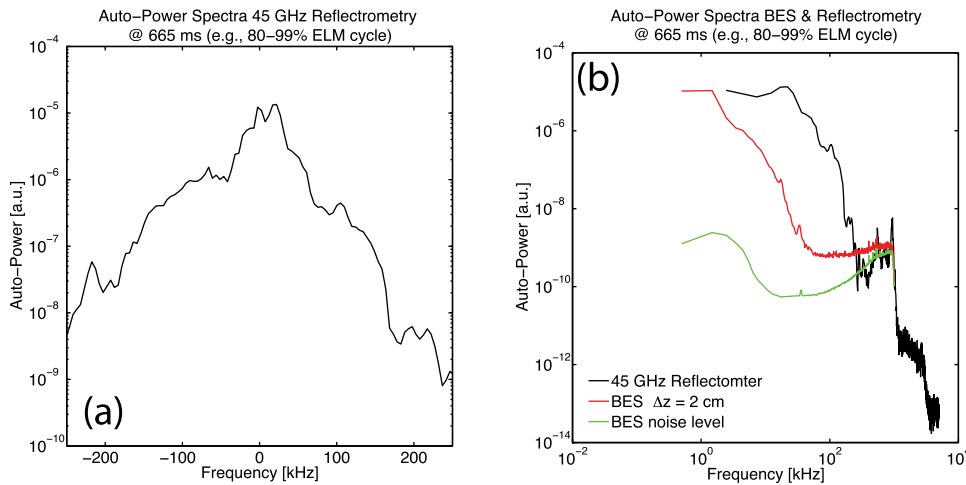
FIG. 3. (a) Examples of power spectra displaying broadband fluctuations in one of the reflectometer channels (45 GHz). (b) Comparison of the power spectra between the BES and the reflectometer showing similar broadband fluctuations.

$\langle k^r_{turb} \rangle$ representing the observed quantities. Given the measured coherency, fluctuation levels less than 5% reproduce the experimental data. Furthermore, this map provides us with information on potential impact of the large density fluctuations such as blobs on the measured correlation. In fact, increasing the fluctuation levels from 1% to 5%, we observe a drop of 40% in coherency, which suggests that for blobs ($\delta n/n \sim 100\%$) the correlation coefficient will drop to the statistical noise level.

Figure 6 shows the simulated correlation function for the case of $\delta n/n \sim 1\%$ and $\lambda^r_{turb} \sim 1.3$ cm, which agrees well with the experimental radial correlation lengths. An important result from the 2D simulations is that we found that λ_{turb} is similar in magnitude to λ^r_{obs} for this set of NSTX data. Great care should be exercised as to avoid generalizing by assuming that λ^r_{obs} is equal to λ_{turb}. Conditions where this equality is met could be the subject of future investigations. In the full wave modelling, the poloidal size of the eddies was chosen to match their radial size. Note that variation in the choice of the poloidal size was found to have minimal effect on the full wave simulation estimates of the radial correlations.[38]

With the 2D full wave modeling indicating that $\lambda^r_{obs} \sim \lambda^r_{turb}$, the evolution of the correlation lengths of both the pedestal top and the steep gradient region is shown in Figure 7. The radial correlation length measurements are

well above the instrument resolution, which is given by the width of the last Airy fringe near the turning point,[32] $W_{Airy} = 0.48 L_n^{1/3} \lambda_0^{2/3}$. Here, λ_0 is the free space wavelength of the probing radiation, and $L_n = |n/\nabla n|$ is the local density gradient scale. Two horizontal lines (see Figure 7) representing the instrument resolution for both the pedestal top and the steep gradient region, show that the measured correlation lengths are well resolved. In Figure 7, it is clearly observed that during the inter-ELM phase, the radial correlation length at the pedestal top increases during the last 50% of the ELM cycle, while the radial correlation length in the steep gradient region shows little variation during the inter-ELM phase. This increase at the pedestal top during the ELM cycle is consistent with a radial expansion of the pressure pedestal width toward the core. In the steep gradient region, on the other hand, while the pedestal width expands during the ELM cycle, the radial correlation length appears to be unaffected and remains smaller than the pressure pedestal width of 3 cm (see Figure 4(a) of Diallo et al.[16]).

Using the ion temperature evaluated at the top of the electron temperature pedestal (440 eV), we estimate the radial correlation lengths displayed in Figure 7 to span $k^r_{turb} \rho_i^{ped}$ (where $\rho_i^{ped} \sim 9$ mm is the ion gyroradius at the pedestal top and $k^r_{turb} = 2/\lambda^r_{turb}$) ranging from 0.2 to 0.7. This range in $k^r_{turb} \rho_i^{ped}$ is estimated to be accurate within 20% if systematic errors are accounted for in the estimates of the
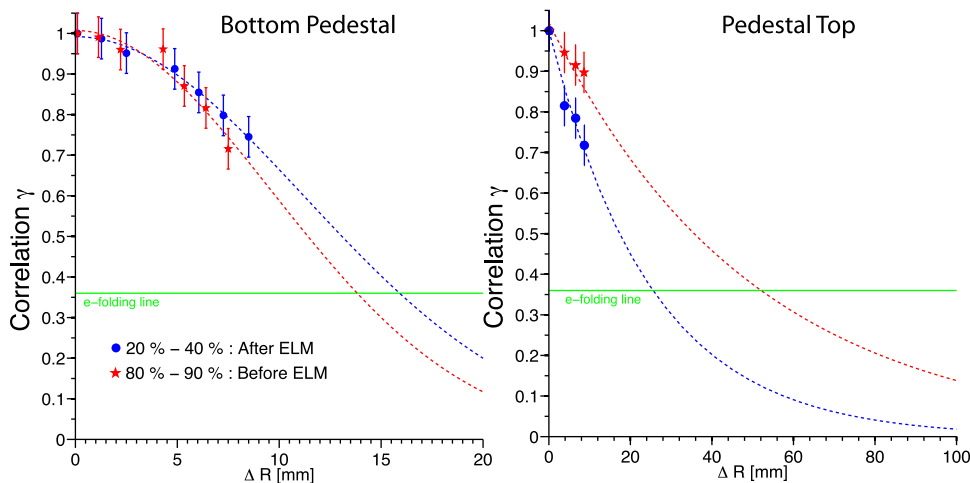

FIG. 4. Correlation functions early (circles) and late (stars) in the ELM cycle in the steep gradient region or bottom of the pedestal (left) and at the pedestal top (right). Note that the correlation lengths are determined from the crossing of the correlation function (dotted lines) with e-folding horizontal lines.
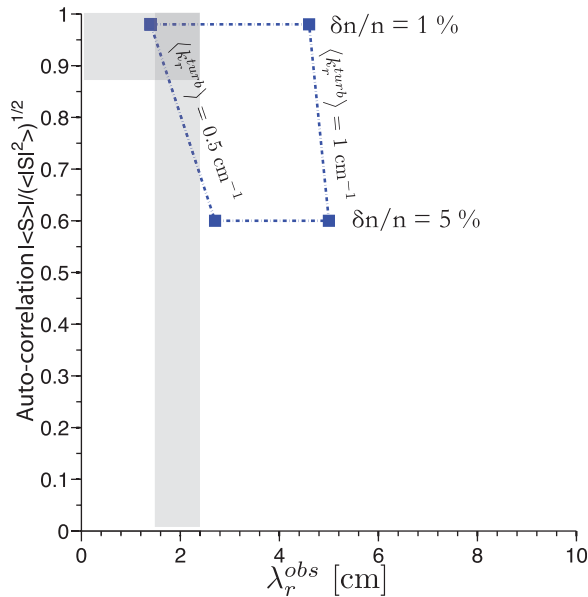
FIG. 5. Turbulence parameters mapping as a function of measured quantities. The shaded regions highlight the measured values in the steep gradient region.

spatial separation between channels due to the choice of the fit functions are accounted. We assumed throughout this paper a Gaussian k-spectrum enabling the link to the correlation length $2/k$. For completeness in the estimate of $k_\perp$, the poloidal component is determined using the BES system as discussed in the section below.

B. Characterization of the poloidal spatial structure near the pedestal top

For a complete description of the pedestal region fluctuation characterizations, a measure of the spatial structure in the poloidal direction, in addition to the propagation direction, is determined. Long-wavelength, localized density fluctuations are determined using the BES system,[31] which measures Doppler shifted collisionally excited neutral beam
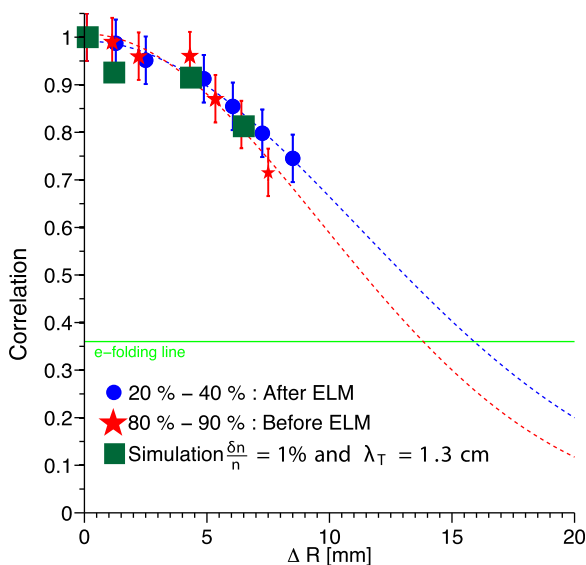

FIG. 6. Simulated correlation function using the 2D full wave simulation overlaid onto experimentally measured correlation function.
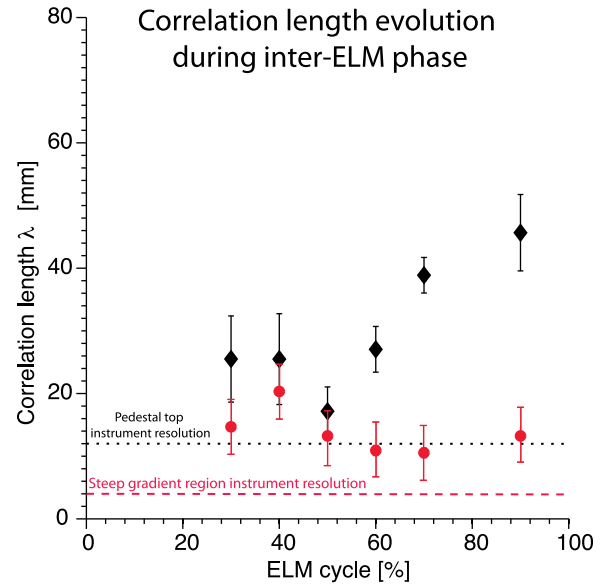

FIG. 7. Evolution of the radial correlation length in the pedestal regions: pedestal top (diamond) and steep gradient (circle). The horizontal dotted and dashed lines represent the instrument resolutions at the pedestal top and in the steep gradient region, respectively (see text for details).

D_α emission. The light intensity is related to the local density fluctuations through the atomic physics of beam atom excitation. Note that contrary to the correlation reflectometry which requires a 2D modeling to unfold the turbulence correlation lengths, BES measurements provide more direct estimates of the turbulent correlation lengths assuming that these lengths are large compared with the poloidal resolution.

A poloidal array of four BES channels is located at $R = 1.40 \text{ m}$ with a spatial resolution of $\Delta z \sim 2.5 \text{ cm}$. The poloidal correlation length is determined from the correlation function between spatially separated points near the pedestal top. The advection velocity (in the laboratory frame) is computed from the associated time delay at peak correlation. These broadband fluctuations are observed over the frequency range 8-50 kHz as shown in Figure 8. The lower end of this frequency range was chosen to minimize the low frequency neutral beam fluctuations on the poloidal measurements. Figure 9 displays the evolution of the poloidal correlation during the inter-ELM phase. This shows modest change of the poloidal length ($\sim 13 \, \rho_i^{\text{ped}}$) during the ELM cycle. Combining the radial and poloidal correlation lengths at the pedestal top, the relevant spatial scales ($k_\perp \rho_i^{\text{ped}}$) of microturbulence range from 0.2 to 0.7. Furthermore, the difference in spatial scale in the poloidal and radial directions points to a strong anisotropy of the microturbulence.

Figure 10 shows both the inter-ELM group velocities determined from the time lags between BES channels and the $E_r \times B$ at the pedestal top which is inferred from the force-balance equation of the carbon ion distribution from the CHERS system. The BES velocities represent the advection velocities of the eddies. In order to relate these velocities with the propagation velocities, we account for the $E_r \times B$ velocities at the pedestal top ($R \sim 1.40 \text{ m}$). It is clear from Figure 10 that the $E_r \times B$ velocities are measurably smaller
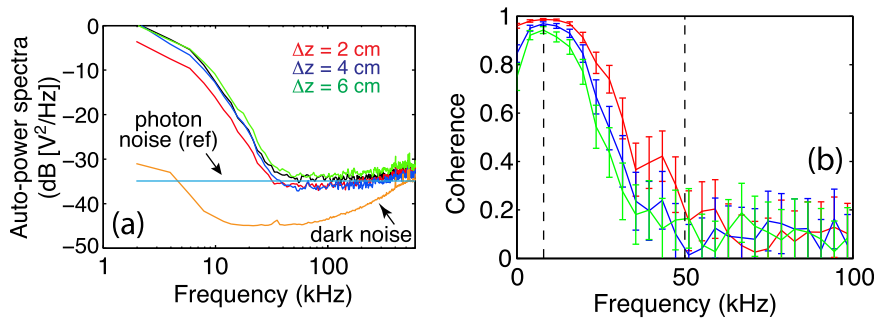
FIG. 8. Example of BES fluctuation spectra for three channels with the vertical lines indicating the region of computed correlations: (a) auto-power spectra, (b) coherence spectra.

at the pedestal top than BES-determined group velocities, and in the opposite direction. This is contrary to the observations in the DIIID tokamaks where both group velocities and $E_r \times B$ velocities are large and in the same direction.[21] The propagation velocities, determined from $v_{E_r \times B}^{CHERS} + v_{group}^{BES}$, clearly show propagation in the ion diamagnetic direction and are consistent with propagation velocities inferred from Figure 5 of Yan et al.[21] Note that positive velocity represents propagation in the ion diamagnetic direction while negative velocity indicates a propagation in the electron diamagnetic direction (see Figure 10). Differences observed between the absolute individual values of $v_{E_r \times B}^{CHERS}$ and v_{group}^{BES} between DIIID and the NSTX are not yet well understood but could highlight the aspect ratio differences.

The edge density fluctuations in the pedestal region during the ELM cycle clearly show strongly anisotropic fluctuations and spatial scales indicative of ion-scale turbulence propagating in the ion diamagnetic direction. Given these measurements of the pedestal turbulence during the inter-ELM phase, it is clear that the fluctuations exhibit ion-scale microturbulence compatible with ITG (including hybrids) and/or KBM instabilities.

IV. SUMMARY AND DISCUSSION

In summary, we have extended studies of the pedestal structure during the inter-ELM phase to further understand the limiting mechanisms during the pedestal height dynamics. It has been proposed that the pressure gradient is limited by the KBM[7] during the continuous increase of the pedestal height and width. While a direct test of this mechanism is difficult to perform with the current data, we have characterized the evolution of the spatial structure of broadband fluctuations present during the inter-ELM cycle.

Specifically, detailed measurements of density between the and fluctuations spatial structure in the pedestal top and steep gradient regions during the ELM cycle are reported. Using diagnostics probing density fluctuations in both poloidal and radial directions, spatial scales at the pedestal top are observed and found consistent with ion-scale microturbulence propagating in the ion diamagnetic directions.

Two theoretical candidates consistent with the measured ion scale turbulence are the ITG/TEM and KBM instabilities. Generally both instabilities exist at similar spatial scales and are often expected to propagate in the ion diamagnetic drift direction. Distinguishing these modes experimentally is challenging, although the KBM is expected to exhibit a linear threshold at finite β.[39,40] A combination of transport and turbulence measurements, coupled with linear and nonlinear simulations, could help clarify which mode may be most important. We also note that microtearing[26,41] and electron temperature gradient (ETG) instabilities[41,42] can also be
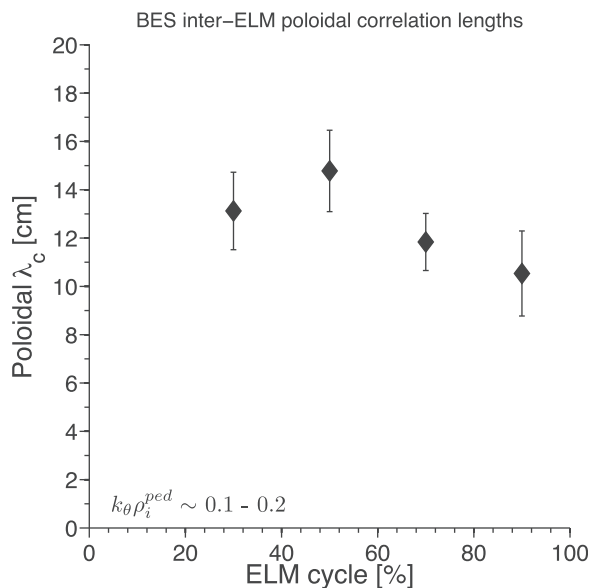

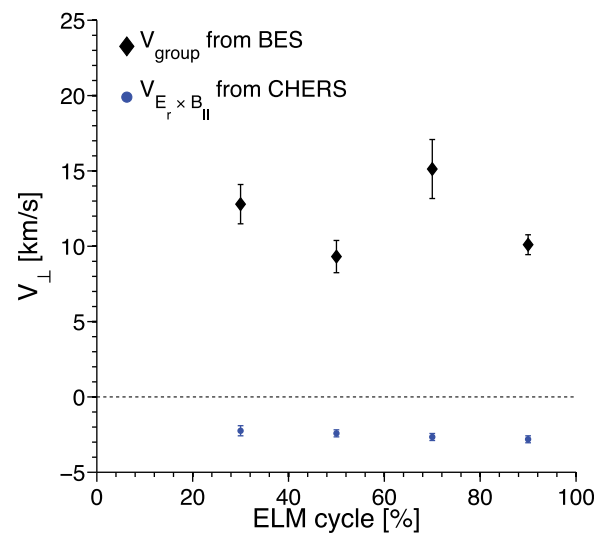FIG. 9. Inter-ELM poloidal correlation length evolution measured using the BES system.

FIG. 10. Poloidal velocity evolution. The diamond symbols represent the group velocities determined using the BES system projected in the perpendicular direction $\hat{e}_r \times \hat{b}$, where $\hat{b}$ is the unit vector of **B**. The circle symbols indicate the $E_r \times B$ velocities obtained from the CHERS system at the pedestal top (R ∼ 1.40 m). See text for details.
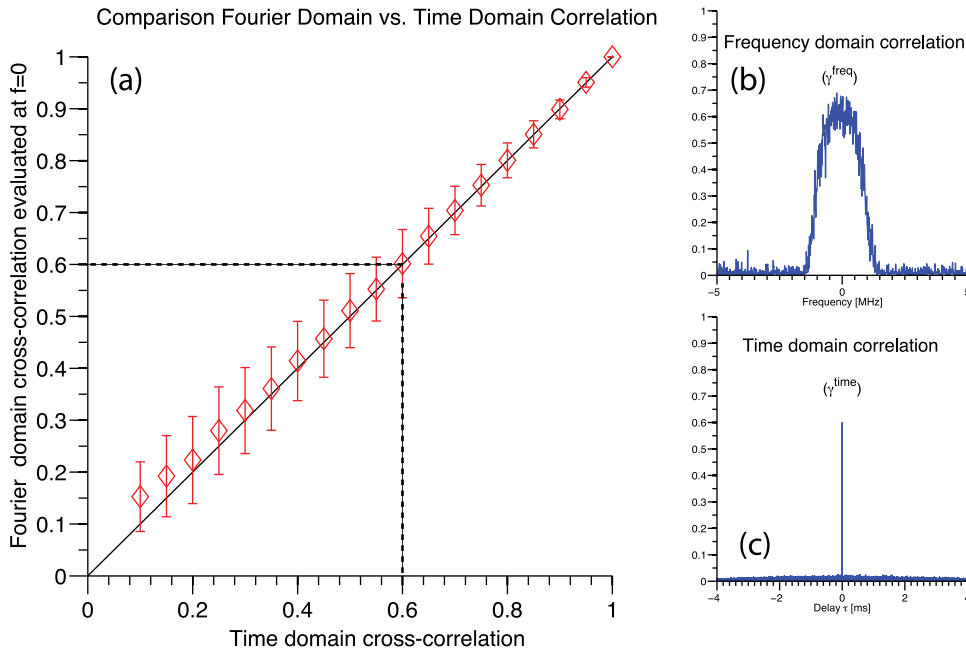
FIG. 11. (a) Comparison between the Fourier domain approach and the time domain correlation. (b), (c) In the right panel, two traces are showing the correlation in time domain and frequency domain for the specific case when the correlation value is 0.6.

unstable near the plasma edge. However, they are only expected to cause significant electron thermal transport and negligible transport in other thermal channels. Furthermore, reflectometry and BES are unlikely to be sensitive to them as microtearing density perturbations are predicted to be very narrow ($\sim \rho_i$) and ETG turbulence exists entirely at electron scales ($< \rho_i$), which could be probed using high-k diagnostics. Both flux-tube, δf (GS2)[43] and global full-f (XGC1)[44] gyrokinetic simulations are being pursued to study the linear stability and turbulence characteristics in the NTSX pedestal region. Such first principle simulations, coupled with synthetic diagnostics, will be required to compare to measurements using correlation reflectometry and BES.

Experiments which could help distinguish between ITG and KBM include pellet injections and careful heating using ECH heating in the pedestal region. Pellet injections could provide enough fueling of the pedestal region to observe variations of the density gradient. With such variations of the density gradient, one will obtain an effective scan of β_e. Similarly, EC heating of the pedestal region could provide a scan of β_e via variations of the temperature gradient. In both types of experiments (via density or temperature gradient changes), KBM could be distinguished from ITG- a ubiquitous instability. These experiments will require fast measurements of the density fluctuations (BES or reflectometry) to probe fluctuations in the pedestal regions while the pressure gradient varies.

ACKNOWLEDGMENTS

APPENDIX: CROSS-CORRELATION IN TIME DOMAIN AND FOURIER DOMAIN

In this appendix, we show that the cross-correlation in the time domain between two signals $f(t)$ and $g(t)$ is equivalent to correlation evaluated in frequency domain. The cross-correlation in time domain, γ^{time}, is defined as the integral over all delays τ of the convolution between two signals $R_{fg}(\tau) = f(t) \otimes g(t-\tau)$ with $\otimes$ is the convolution operator and the two signals $f(t)$ and $g(t)$ are finite in a time interval $[0, T]$ and zero outside. The equivalence can be shown easily

$$
\begin{aligned}
\gamma^{time} &= \int f(t) \otimes g(t-\tau) d\tau = \iint f^*(t) g(t-\tau) dt d\tau \\
&= \iiint F^*(\omega) e^{i\omega t} d\omega \int G(\omega') e^{i\omega'(t-\tau)} d\omega' dt d\tau \\
&= \iiint F^*(\omega) G(\omega') e^{i\omega' t} \underbrace{\left[\int e^{i(\omega-\omega')t} dt \right]}_{\delta(\omega-\omega')} d\omega' d\omega d\tau \\
&= \iint F^*(\omega) G(\omega) e^{i\omega\tau} d\tau d\omega = \int F^*(\omega) G(\omega) \delta(\omega) d\omega \\
&= F^*(0) G(0) = \gamma^{freq}.
\end{aligned}
$$

Here, γ^{freq} is the correlation in frequency space; and F and G are the Fourier transforms of f and g, respectively. Note that ω is the reciprocal of the delay time τ. Furthermore, in Figure 11, we show this equivalence between correlation in time and Fourier domain given two randomly distributed signals by varying the correlation value between the two signals.

[1] ITER Physics Basis Editors, Nucl. Fusion **39**, 2137 (1999).

[2] J. Kinsey, G. Staebler, J. Candy, R. Waltz, and R. Budny, Nucl. Fusion **51**, 083001 (2011).

[3] J. W. Connor, R. J. Hastie, H. R. Wilson, and R. L. Miller, Phys. Plasmas **5**, 2687 (1998).

[4] H. R. Wilson, P. B. Snyder, G. T. A. Huysmans, and R. L. Miller, Phys. Plasmas **9**, 1277 (2002).

[5] P. B. Snyder, H. R. Wilson, J. R. Ferron, L. L. Lao, A. W. Leonard, T. H. Osborne, A. D. Turnbull, D. Mossessian, M. Murakami, and X. Q. Xu, Phys. Plasmas **9**, 2037 (2002).

[6] P. B. Snyder, R. J. Groebner, A. W. Leonard, T. H. Osborne, and H. R. Wilson, Phys. Plasmas **16**, 056118 (2009).

[7] P. Snyder, R. Groebner, J. Hughes, T. Osborne, M. Beurskens, A. Leonard, H. Wilson, and X. Xu, Nucl. Fusion **51**, 103016 (2011).

[8] M. Ono, S. Kaye, Y.-K. Peng, G. Barnes, W. Blanchard, M. Carter, J. Chrzanowski, L. Dudek, R. Ewig, D. Gates, R. Hatcher, T. Jarboe, S. Jardin, D. Johnson, R. Kaita, M. Kalish, C. Kessel, H. Kugel, R. Maingi, R. Majeski, J. Manickam, B. McCormack, J. Menard, D. Mueller, B. Nelson, B. Nelson, C. Neumeyer, G. Oliaro, F. Paoletti, R. Parsells, E. Perry, N. Pomphrey, S. Ramakrishnan, R. Raman, G. Rewoldt, J. Robinson, A. Roquemore, P. Ryan, S. Sabbagh, D. Swain, E. Synakowski, M. Viola, M. Williams, J. Wilson, and NSTX Team, Nucl. Fusion **40**, 557 (2000).

[9] R. Maingi, C. Bush, E. Fredrickson, D. Gates, S. Kaye, B. LeBlanc, J. Menard, H. Meyer, D. Mueller, N. Nishino, A. Roquemore, S. Sabbagh, K. Tritz, S. Zweben, M. Bell, R. Bell, T. Biewer, J. Boedo, D. Johnson, R. Kaita, H. Kugel, R. Maqueda, T. Munsat, R. Raman, V. Soukhanovskii, T. Stevenson, and D. Stutman, Nucl. Fusion **45**, 1066 (2005).

[10] D. Mansfield, H. Kugel, R. Maingi, M. Bell, R. Bell, R. Kaita, J. Kallman, S. Kaye, B. LeBlanc, D. Mueller, S. Paul, R. Raman, L. Roquemore, S. Sabbagh, H. Schneider, C. Skinner, V. Soukhanovskii, J. Timberlake, J. Wilgen, and L. Zakharov, J. Nucl. Mater. **390–391**, 764–767 (2009).

[11] M. G. Bell, H. W. Kugel, R. Kaita, L. E. Zakharov, H. Schneider, B. P. LeBlanc, D. Mansfield, R. E. Bell, R. Maingi, S. Ding, S. M. Kaye, S. F. Paul, S. P. Gerhardt, J. M. Canik, J. C. Hosea, G. Taylor, and NSTX Research Team, Plasma Phys. Controlled Fusion **51**, 124054 (2009).

[12] H. Kugel, D. Mansfield, R. Maingi, M. Bell, R. Bell, J. Allain, D. Gates, S. Gerhardt, R. Kaita, J. Kallman, S. Kaye, B. LeBlanc, R. Majeski, J. Menard, D. Mueller, M. Ono, S. Paul, R. Raman, A. Roquemore, P. Ross, S. Sabbagh, H. Schneider, C. Skinner, V. Soukhanovskii, T. Stevenson, J. Timberlake, W. Wampler, J. Wilgren, and L. Zakharov, J. Nucl. Mater. **390–391**, 1000 (2009).

[13] R. Maingi, T. H. Osborne, B. P. LeBlanc, R. E. Bell, J. Manickam, P. B. Snyder, J. E. Menard, D. K. Mansfield, H. W. Kugel, R. Kaita, S. P. Gerhardt, S. A. Sabbagh, F. A. Kelly, and NSTX Research Team, Phys. Rev. Lett. **103**, 075001 (2009).

[14] D. P. Boyle, R. Maingi, P. B. Snyder, J. Manickam, T. H. Osborne, R. E. Bell, B. P. LeBlanc, and NSTX Team, Plasma Phys. Controlled Fusion **53**, 105011 (2011).

[15] J. M. Canik, R. Maingi, S. Kubota, Y. Ren, R. E. Bell, J. D. Callen, W. Guttenfelder, H. W. Kugel, B. P. LeBlanc, T. H. Osborne, and V. A. Soukhanovskii, Phys. Plasmas **18**, 056118 (2011).

[16] A. Diallo, R. Maingi, S. Kubota, A. Sontag, T. Osborne, M. Podestà, R. Bell, B. LeBlanc, J. Menard, and S. Sabbagh, Nucl. Fusion **51**, 103031 (2011).

[17] R. J. Groebner, T. H. Osborne, A. W. Leonard, and M. E. Fenstermacher, Nucl. Fusion **49**, 085037 (2009).

[18] A. Kirk, G. F. Counsell, G. Cunningham, J. Dowling, M. Dunstan, H. Meyer, M. Price, S. Saarelma, R. Scannell, M. Walsh, H. R. Wilson, and MAST Team, Plasma Phys. Controlled Fusion **49**, 1259 (2007).

[19] X. Garbet, Y. Idomura, L. Villard, and T. Watanabe, Nucl. Fusion **50**, 043002 (2010).

[20] K. Burrell, T. Osborne, P. Snyder, W. West, M. Fenstermacher, R. Groebner, P. Gohil, A. Leonard, and W. Solomon, Nucl. Fusion **49**, 085024 (2009).

[21] Z. Yan, G. R. McKee, R. J. Groebner, P. B. Snyder, T. H. Osborne, and K. H. Burrell, Phys. Rev. Lett. **107**, 055004 (2011).

[22] D. Dickinson, S. Saarelma, R. Scannell, A. Kirk, C. M. Roach, and H. R. Wilson, Plasma Phys. Controlled Fusion **53**, 115010 (2011).

[23] W. Guttenfelder, J. Candy, S. M. Kaye, W. M. Nevins, E. Wang, J. Zhang, R. E. Bell, N. A. Crocker, G. W. Hammett, B. P. LeBlanc, D. R. Mikkelsen, Y. Ren, and H. Yuh, Phys. Plasmas **19**, 056119 (2012).

[24] Z. Yan, G. R. McKee, R. J. Groebner, P. B. Snyder, T. H. Osborne, M. N. Beurskens, and K. H. Burrell, Phys. Plasmas **18**, 056117 (2011).

[25] J. Candy and R. Waltz, J. Comput. Phys. **186**, 545 (2003).

[26] W. Guttenfelder, J. Candy, S. M. Kaye, W. M. Nevins, E. Wang, J. Zhang, R. E. Bell, N. A. Crocker, G. W. Hammett, B. P. LeBlanc, D. R. Mikkelsen, Y. Ren, and H. Yuh, Phys Plasmas **19**, 056119 (2012)

[27] B. P. LeBlanc, R. E. Bell, D. W. Johnson, D. E. Hoffman, D. C. Long, and R. W. Palladino, Rev. Sci. Instrum. **74**, 1659 (2003).

[28] R. E. Bell, R. Andre, S. M. Kaye, R. A. Kolesnikov, B. P. LeBlanc, G. Rewoldt, W. X. Wang, and S. A. Sabbagh, Phys. Plasmas **17**, 082507 (2010).

[29] T. H. Osborne, P. B. Snyder, K. H. Burrell, T. E. Evans, M. E. Fenstermacher, A. W. Leonard, R. A. Moyer, M. J. Schaffer, and W. P. West, J. Phys.: Conf. Ser. **123**, 012014 (2008).

[30] N. A. Crocker, W. A. Peebles, S. Kubota, J. Zhang, R. E. Bell, E. D. Fredrickson, N. N. Gorelenkov, B. P. LeBlanc, J. E. Menard, M. Podestà, S. A. Sabbagh, K. Tritz, and H. Yuh, Plasma Phys. Controlled Fusion **53**, 105001 (2011).

[31] D. R. Smith, H. Feder, R. Feder, R. J. Fonck, G. Labik, G. R. McKee, N. Schoenbeck, B. C. Stratton, I. Uzun-Kaymak, and G. Winz, Rev. Sci. Instrum. **81**, 10D717 (2010).

[32] R. Nazikian, G. J. Kramer, and E. Valeo, Phys. Plasmas **8**, 1840 (2001).

[33] J. S. Bendat and A. G. Piersol, Random Data: Analysis and Measurement Procedures (John Wiley and Sons, 1971).

[34] E. Mazzucato, Rev. Sci. Instrum. **69**, 2201 (1998).

[35] E. J. Valeo, G. J. Kramer, and R. Nazikian, Plasma Phys. Controlled Fusion **44**, L1 (2002).

[36] M. Gilmore, W. A. Peebles, and X. V. Nguyen, Plasma Phys. Controlled Fusion **42**, 655 (2000).

[37] G. J. Kramer, R. Nazikian, and E. Valeo, Rev. Sci. Instrum. **74**, 1421 (2003).

[38] R. Nazikian, K. Shinohara, G. J. Kramer, E. Valeo, K. Hill, T. S. Hahm, G. Rewoldt, S. Ide, Y. Koide, Y. Oyama, H. Shirai, and W. Tang, Phys. Rev. Lett. **94**, 135002 (2005).

[39] R. E. Waltz, Phys. Plasmas **17**, 072501 (2010).

[40] P. Snyder, "Gyrofluid theory and simulation of electromagnetic turbulence and transport in tokamak plasmas," Ph.D. thesis (Princeton University, 1999).

[41] D. Told, F. Jenko, P. Xanthopoulos, L. D. Horton, E. Wolfrum, and A. U. Team, Phys. Plasmas **15**, 102306 (2008).

[42] F. Jenko, D. Told, P. Xanthopoulos, F. Merz, and L. D. Horton, Phys. Plasmas **16**, 055901 (2009).

[43] W. Dorland, F. Jenko, M. Kotschenreuther, and B. N. Rogers, Phys. Rev. Lett. **85**, 5579 (2000).

[44] S. Ku, C. Chang, and P. Diamond, Nucl. Fusion **49**, 115021 (2009).